JACS
JOURNAL OF THE AMERICAN CHEMICAL SOCIETY
pubs.acs.org/JACS
Article

Strategic Modulation of Polarity and Viscosity Sensitivity of Bimane Molecular Rotor-Based Fluorophores for Imaging α-Synuclein

Yarra Venkatesh,* Karthik B. Narayan, Tobias Baumgart, and E. James Petersson*

Cite This: J. Am. Chem. Soc. 2025, 147, 15115−15125
Read Online
ACCESS | Metrics & More | Article Recommendations | Supporting Information

ABSTRACT: Molecular rotor-based fluorophores (RBFs) that are target-selective and sensitive to both polarity and viscosity are valuable for diverse biological applications. Here, we have designed next-generation RBFs based on the underexplored bimane fluorophore either through a change in aryl substitution or varying π-linkages between the rotatable electron donors and acceptors to produce red-shifted fluorescence emissions with large Stokes shifts. RBFs exhibit a twisted intramolecular charge transfer mechanism that enables control of polarity and viscosity sensitivity as well as target selectivity. These features enable their application in (1) turn-on fluorescent detection of α-synuclein (αS) fibrils, a hallmark of Parkinson's disease, including amplified fibrils from patient samples; (2) monitoring early misfolding and oligomer formation during αS aggregation; and (3) selective imaging of αS condensates formed by liquid−liquid phase separation. In all three cases, we show that our probes have high levels of selectivity for αS compared to other aggregating proteins. These properties enable one to study the interplay of αS and tau in amyloid aggregation and the mechanisms underlying neurodegenerative disorders.

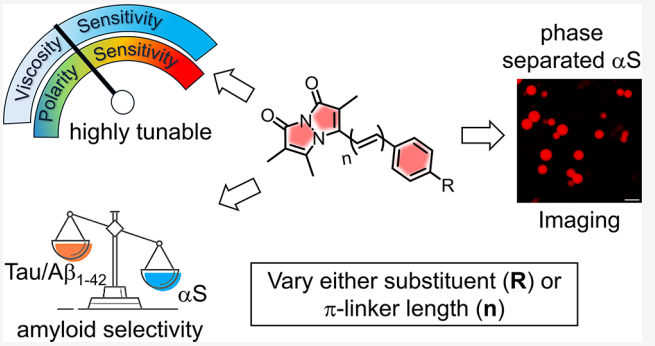

INTRODUCTION

Fluorescence imaging is a crucial tool for studying complex biological pathways, diagnosing diseases, and gaining detailed insights into molecular and cellular processes.[1−3] This technique requires precise labeling of fluorescent probes to visualize biological entities and track interactions in real time. Over the past two decades, several labeling strategies have been developed that include fluorescent proteins like GFP and genetically encodable tags (e.g., HaloTag, SNAP-Tag, and Spinach).[4−6] However, these often have limitations due to their large size that can interfere with the native function of the biological molecules that are intended to be studied.[7] Small organic dyes can be directly attached to proteins or DNA/RNA through chemical conjugation methods, but these methods are either restricted to in vitro or require manipulation of cellular machinery through methods like genetic code expansion, making them hard to apply in native biological samples.[1] To overcome these limitations and enable direct fluorescence imaging without the need for extensive labeling strategies, there is a need to develop fluorescent probes that are highly target selective.

Molecular rotor-based fluorophores (RBFs) using the twisted intramolecular charge transfer (TICT) mechanism find applications in biological imaging, membrane chemistry, and material science.[8−10] Typically, RBFs feature an electron donor, an electron acceptor, and a linkage that facilitates charge transfer. In solvents that allow rotation between the donor and acceptor, these fluorophores adopt twisted conformations in excited states, leading to rapid ICT and effective fluorescence quenching. Restricted rotation enhances fluorescence by reducing nonradiative decay, making RBFs valuable as biosensors in viscous environments.

Recently, small-molecule-based RBFs have emerged as powerful tools to study protein misfolding and aggregation, which can occur due to genetic mutations, post-translational modifications, exogenous toxins, and cellular stresses. Protein misfolding and amyloid fibril formation have been associated with Alzheimer's disease (AD), Parkinson's disease (PD), and many other neurodegenerative disorders.[11] Thioflavin-T (ThT), an exemplar RBF, is widely used for the detection of a variety of protein aggregates.[12,13] However, ThT and many other RBFs primarily turn on in the presence of mature fibrils, and are weakly fluorescent with early aggregation species such as protein condensates or nonfibrillar oligomers.[14−17] Detecting these early species is critical for understanding the full scope of protein aggregation pathology.

In a recent development, Zhang and co-workers introduced RBFs derived from ThT with extended π-rich linkages (Figure

Received: December 15, 2024
Revised: April 9, 2025
Accepted: April 10, 2025
Published: April 22, 2025

https://doi.org/10.1021/jacs.4c17933
J. Am. Chem. Soc. 2025, 147, 15115−15125

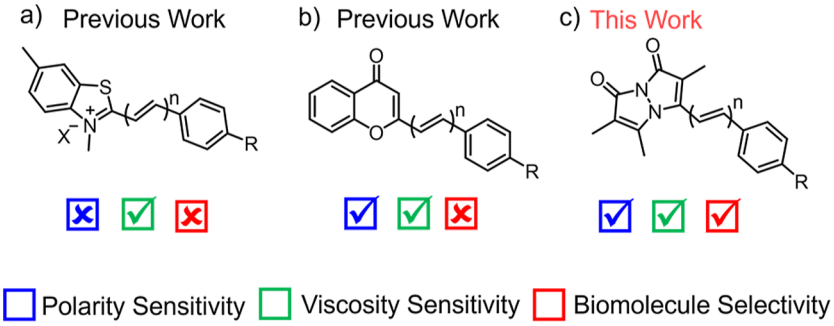

Figure 1. Molecular rotor-based fluorophores (RBFs). (a) Benzothiazolium-based RBFs with viscosity sensitivity. (b) Chromone-based RBFs with dual sensitivities to polarity and viscosity. Here "*n*" denotes π-linker length between donor and acceptor moieties, n = 0, 1, and 2 and R = NMe_2. (c) Bimane-based RBFs exhibit dual sensitivities to polarity and viscosity with high biomolecule selectivity. Here, n = 1 or 2 and R = NH_2, NHMe, NMe_2, azetidine, and morpholine.

Scheme 1. Design and Synthesis of RBFs 3a−e and 4a with Either Varied Aryl Substituents or Extended π-Rich Linkages[a]

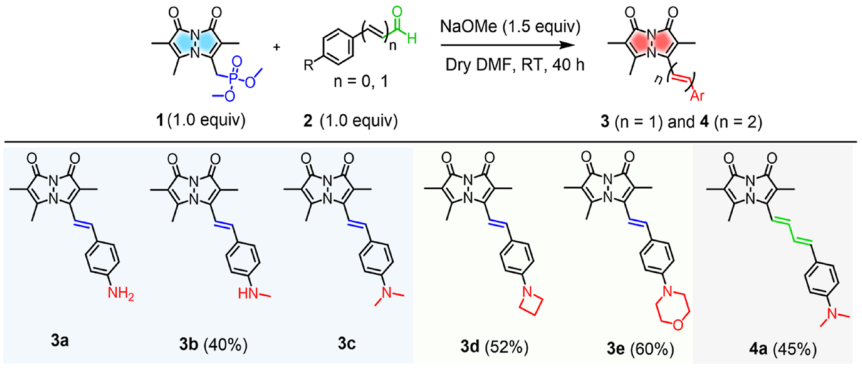

[a]Synthesis of RBFs **3a** and **3c** was previously reported

1a).[18] This innovation enabled the control of viscosity sensitivity by changing the rotational energy barrier (E_a), thereby inducing fluorescence turn-on through a restricted TICT mechanism, enabling selective imaging of protein oligomers and aggregates using their AggTag method (where HaloTag is fused to a protein of interest and labeled with HaloTag ligand modified attached to the fluorophore).[19]

Subsequently, Liu's laboratory demonstrated that polarity sensitivity could be regulated by extending the conjugation length derived from a chromone acceptor moiety (Figure 1b).[20] This approach controlled both polarity and viscosity sensitivity through changes in ICT and E_a, respectively. The resulting probes offered insights into the polarity of aggregated proteins via AggTag labeling in live cells. Despite the advancements of the AggTag method, the large size of HaloTag (33 kDa) has the potential to disrupt disordered amyloidogenic proteins like α-synuclein (αS) and tau that can be sensitive to single point mutations.[21,22] A key challenge in studying αS aggregation is the lack of tools to study early species, such as those involved in misfolding and liquid−liquid phase separation (LLPS),[23−25] limiting their application in early disease diagnosis. The sensitivity of RBFs developed by Zhang's lab is restricted to oligomeric species and fibrils. To detect low-viscosity species such as early aggregates or LLPS, novel fluorescent probes with adjustable sensitivity are needed. Additionally, the lack of intrinsic protein selectivity requires the use of HaloTag and limits studying unmodified proteins in neurodegenerative diseases that involve coaggregation of multiple amyloidogenic proteins.

In this study, we report the chemical modification of RBFs based on the underexplored bimane[26,27] fluorophore by either changing the aryl substituent or installing π-rich bridges between the two rotational moieties (Figure 1c). These chemical modifications demonstrate new mechanisms to control RBF polarity sensitivity through enhanced ICT character and to control viscosity sensitivity by altering E_a for the transition between the fluorescent planar excited state and the dark twisted state. The modifications also enhance photophysical properties, such as red-shifting absorption in the visible region. These features enable use as "turn-on" fluorescent probes to detect αS fibrillar aggregates, a hallmark of PD.[28] Structural variations in RBFs improve the selectivity for αS fibrils versus other amyloidogenic proteins. This selectivity enables detection of αS fibrils amplified from patient samples. Finally, the sensitivity of our RBFs to low viscosity early aggregation species is used in the fluorescence imaging of αS protein LLPS condensates.

RESULTS AND DISCUSSION

Rational Design of RBFs. RBFs **3a** (R = NH_2, n = 1) and **3c** (R = NMe_2, n = 1) are stilbene-type analogues that feature a methine group between the electron-donating aryl group and the electron-accepting bimane fluorophore (D−π−A system). Recently, they have been demonstrated as selective fluorogenic probes for detecting amyloid fibrils.[29] To further investigate the bimane-based D−π−A system, we modified either the aryl substituent (R) or the π-linker length (n) between the donor and acceptor moieties. To generalize this system, we introduced substituents with varying electron-donating capaci-

https://doi.org/10.1021/jacs.4c17933
J. Am. Chem. Soc. 2025, 147, 15115−15125

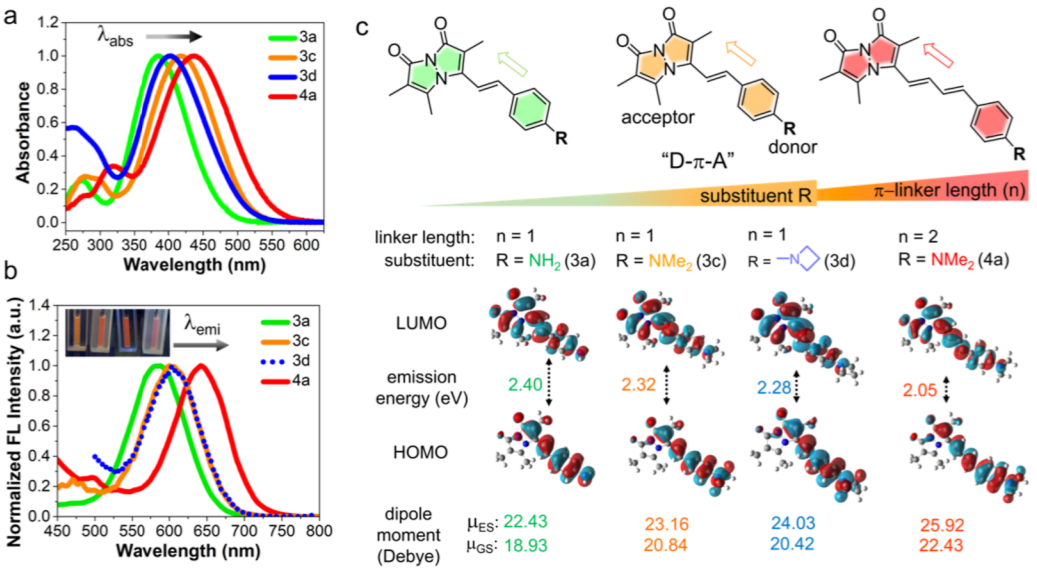

Figure 2. Photophysical properties of RBFs with variations in the aryl substitution (R) or π-linker length (n). (a) Normalized absorption spectra and (b) normalized fluorescence spectra of **3a**, **3c**, **3d**, and **4a**, measured with excitation at their optimal absorption maximum. Inset: photographs of probes (25 μM) under a UV lamp at 365 nm in CH_3CN/PBS buffer (50:50 v/v) at pH 7.4. (c) Top: schematic representation of the bimane probes showing "push–pull" D–π–A type systems; D: donor, π: spacer, and A: acceptor. Bottom: TD-DFT calculated fluorescence emission energy from the S_1 excited state back to the S_0 ground S_0 state of **3a**, **3c**, **3d**, and **4a** in water and the calculated dipole moments of S_0 and S_1 in water, supports the enhanced ICT character from **3a** to **3c–d** to **4a**.

Table 1. Photophysical Properties of RBFs 3a–3e and 4a

RBF dye	substituent (Ph-R)	absorbance λ_{abs}[a] (nm)	emission λ_{em}[b] (nm)	ε[c] (M^{-1} cm^{-1})	Stokes shift[d] (nm)	Fluorescence QY[e] (%)		HOMO–LUMO gap[g] (eV)
						CH_3CN/PBS	CH_3CN[f]	
3a	NH_2	385	583	30800	198	0.7	1.5	3.429
3b	NHMe	399	591	26400	192	0.5	2.0	
3c	NMe_2	418	604	30400	186	0.5	7.3	3.172
3d	Az	403	605	30700	202	0.5	8.1	3.209
3e	Mor	386	603	29600	217	1.0	6.9	3.346
4a[h]	NMe_2	436	640	36700	204	0.6	13.5	2.872

[a]Maximum absorption wavelength. [b]Maximum emission wavelength. [c]Molar absorption coefficients (ε) at maximum absorption wavelength. [d]Difference between maximum absorption wavelength and maximum emission wavelength. [e]Fluorescence QY (error limit within ±5). The final concentration of the probe is 25 μM in CH_3CN/PBS at pH 7.4. [f]Fluorescence QY in CH_3CN. [g]HOMO and LUMO energy levels of probes in water were calculated using APF-D/6-311+G (2d,p) DFT calculations. [h]Probe with diene linker.

ties, such as **3b** (R = NHMe, n = 1), along with heterocyclic amines like **3d** (R = azetidine, Az, n = 1) and **3e** (R = morpholine, Mor, n = 1). Next, we anticipated that extending the methine bridge, as in **4a** (R = NMe_2, n = 2), would result in a second-generation bimane probe with improved photophysical properties within the same D–π–A framework. RBFs **3b**, **3d**, **3e**, and **4a** were synthesized via the Horner–Wadsworth–Emmons (HWE) reaction between phosphonate **1** and commercially available aryl aldehydes (**2b**, **2d**, **2e**, and **2c**), following a previously described procedure,[29] in 40–60% yields (Scheme 1). These compounds were characterized by ^1H, ^{13}C NMR, and high-resolution mass spectrometry analysis (Figures S1–S4).

After synthesizing RBFs with varied aryl substituents or linker lengths, we performed photophysical characterization using absorption and fluorescence spectroscopy, comparing them to **3a** and **3c** in a 1:1 mixture of acetonitrile and phosphate buffered saline (PBS). As shown in Figure 2a,b and Table 1, a bathochromic shift in absorption maximum (λ_{abs}) and emission maximum (λ_{em}) was observed with increased electron donation: **3a–3c** (R = NH_2, R = NHMe, R = NMe_2). These experimental λ_{abs} and λ_{em} values align well with density functional theory (DFT) and time-dependent DFT (TD-DFT) calculations for the ground and excited states, respectively (Table 1 and Figure 2c).

Interestingly, RBF **3d** (R = Az, λ_{abs} = 403 nm) showed a hypsochromic shift in λ_{abs} compared to **3c** (R = NMe_2, λ_{abs} = 418 nm), and an even greater blue-shift seen for **3e** (R = Mor, λ_{abs} = 386 nm), which can be explained by the reduced electronic conjugation caused by the higher ionization potential (IP) of the Az (9.04 eV) and Mor (8.88 eV) groups compared to NMe_2 (8.24 eV). This concept is validated by the larger HOMO–LUMO energy gap for **3d** (E = 3.209 eV) and **3e** (E = 3.346 eV) than that for **3c** (R = NMe_2, E = 3.172 eV) (Figure S5). RBFs **3c**, **3d**, and **3e** have comparable red-shifted λ_{em} at ~605 nm, and TD-DFT calculations show similar emission energy (E_{em} = ~2.3 eV).

Excitingly, RBF **4a** with an extended linker (R = NMe_2, n = 2) exhibited a highly red-shifted λ_{abs} at 436 nm and λ_{em} at 640 nm. Again, electronic structure calculations supported our design, showing the lowest HOMO–LUMO energy of E = 2.87 eV and emission energy of E_{em} = 2.05 eV. In general, the

https://doi.org/10.1021/jacs.4c17933
J. Am. Chem. Soc. 2025, 147, 15115–15125

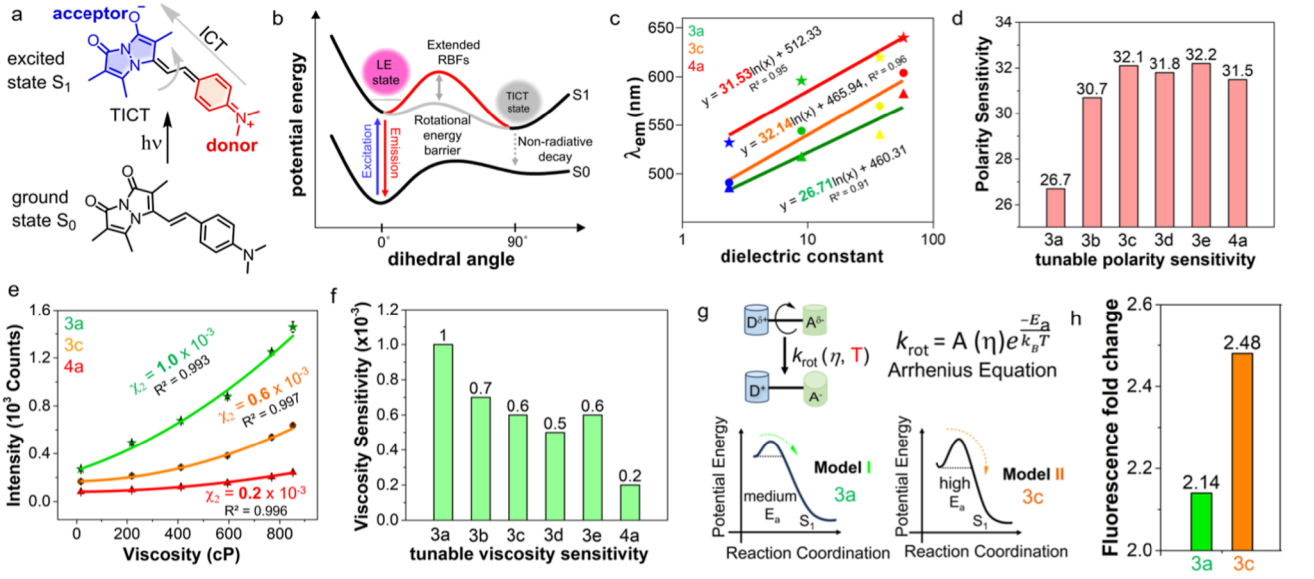

Figure 3. Control of polarity and viscosity sensitivity of RBFs. (a) RBFs with D−π−A system shows the phenomenon of ICT from the donor to the acceptor in the excited state. (b) Jablonski diagram illustrates that an excited fluorophore could return to the ground state either through fluorescence or internal rotation, leading to nonradiative TICT. It shows the effect of aryl substitution (R) or π-rich linkage length (n) to enhance the inherent rotational energy barrier (E_a) of RBFs. (c) Quantitative polarity sensitivity analysis of **3a**, **3c**, and **4a**. (d) Tunable polarity sensitivities of **3a**−**e** and **4a**. (e) Quantitative viscosity sensitivity analysis of **3a**, **3c**, and **4a**. (f) Tunable viscosity sensitivity of **3a**−**e** and **4a**. (g) Temperature dependence reflects the magnitude of E_a. Proposed models suggest that heights of E_a determine the fluorescence intensity pattern in the solvents with different viscosities at different temperatures. Here, two models were conceptualized with moderate and high energy barriers for **3a** and **3c**, respectively. (h) Viscosity dependence fluorescence fold change of **3a** and **3c** at the temperatures of 25 and 42 °C. Probe concentration 25 μM.

experimental photophysical properties agree well with calculated values, as depicted in Tables S2 and S3 and Figure S7. The calculated Stokes shifts for **3a**−**3c** ranged from 186 to 198 nm (Table 1). Notably, **3d** (R = Az) and **3e** (R = Mor) exhibited larger shifts of 202 and 217 nm, respectively, while **4a** showed a shift of 204 nm. The tabulated photophysical properties of **3a**−**e** and **4a** in CH_3CN show blue-shifted λ_{abs} and λ_{em} relative to values in CH_3CN/PBS (Figure S6 and Table S1). Overall, these tunable photophysical properties of RBFs make them promising probes for various biological applications.

Fluorescence quantum yields (QYs) of **3a**−**e** and **4a** in CH_3CN/PBS ranged from 0.5 to 1.0%, compared to 64.6% for phosphonate **1**, due to the TICT effect in polar protic solvents. In contrast, in CH_3CN, the QYs increased with the electron-donating ability of the aryl substituent: 1.5% for **3a** (R = NH_2), 2.0% for **3b** (R = NHMe), and 7.3 ± 0.3% for **3c** (R = NMe_2). For **3d** (R = Az), the QY rose to 8.1 ± 0.2%, likely due to restricted twisting that stabilizes the excited state and reduces TICT formation compared to **3c** (R = NMe_2). Similarly, **3e** (R = Mor) showed a QY of 6.9%. Notably, **4a** (R = NMe_2, n = 2) reached 13.5%, suggesting an even stronger fluorescence turn-on (Table 1 and Figure S8). We assume that modifying the aryl substitution or linker length could control the fluorogenic behavior of RBFs by enhancing E_a or limiting the modes of rotation and isomerization.

Varying the Aryl Substituent or Extended π-Rich Linkages Modulates Polarity Sensitivity of RBFs. We previously demonstrated that probes **3a** and **3c** exhibit polarity and viscosity sensitivity via ICT and TICT mechanisms, respectively (Figure 3a,b).[29] Similarly, RBFs **3b**, **3d**, **3e**, and **4a** display strong solvatochromism, with emission wavelengths ranging from 486−640 nm depending on solvent polarity (Figure S9). Figure 3c depicts the strict linearity between the λ_{em} of **3a**, **3c**, and **4a** and the dielectric constant of solvent, which can enable quantitative analysis of microenvironmental polarity on a protein surface or within cellular compartments. To examine the impact of aryl substituents and linker length on polarity sensitivity, we measured the emission of **3a**−**3e** and **4a** across solvents with varying dielectric constants (Figures 3c and S10). Polarity sensitivity increased with stronger electron donation, as observed in **3a** (26.7), **3b** (30.7), and **3c** (32.1), attributed to the ICT mechanism driven by the dipole moment between electron-donating dialkylaminophenylene groups (R = NH_2, NHMe, and NMe_2) and the electron-withdrawing bimane moiety (Figure 3d). This trend was confirmed by electrostatic potential (ESP) mapping and excited-state dipole moment calculations, showing increased sensitivity from NH_2 to NMe_2 (22.43 for 3a and 23.16 for 3c) (Figures 2c and S11).

RBF **3d** exhibited lower sensitivity (31.8, μ = 20.42 D at ground state) compared to **3c** (32.1, μ = 20.84 D at ground state), due to limited electron donation of the Az with higher IP (9.04 eV), while **3e** with a Mor group (IP = 8.88 eV) showed slightly higher sensitivity (32.2) than **3d** and similar to **3c**, driven by the Mor oxygen's high electronegativity. ESP mapping further confirmed the negative ESP on the Mor oxygen atom that contributes to the increased sensitivity (Figure S11). Interestingly, RBF **4a**, with an extended linker, showed similar overall sensitivity (~31.5, μ = 25.92 D at the excited state) but was more sensitive to solvents with low dielectric constants and less sensitive to those with high dielectric constants. Its solvatochromism was notable, showing a 64 nm λ_{em} shift for **4a** compared to 32−57 nm for **3a**−**e** across solvents with dielectric constants from 2.38 to 8.93 (Figure S12).

Varying the Aryl Substituent or Extended π-Rich Linkages Modulate Viscosity Sensitivity of RBFs. We next examined viscosity sensitivity, which quantifies the

https://doi.org/10.1021/jacs.4c17933
J. Am. Chem. Soc. 2025, 147, 15115−15125

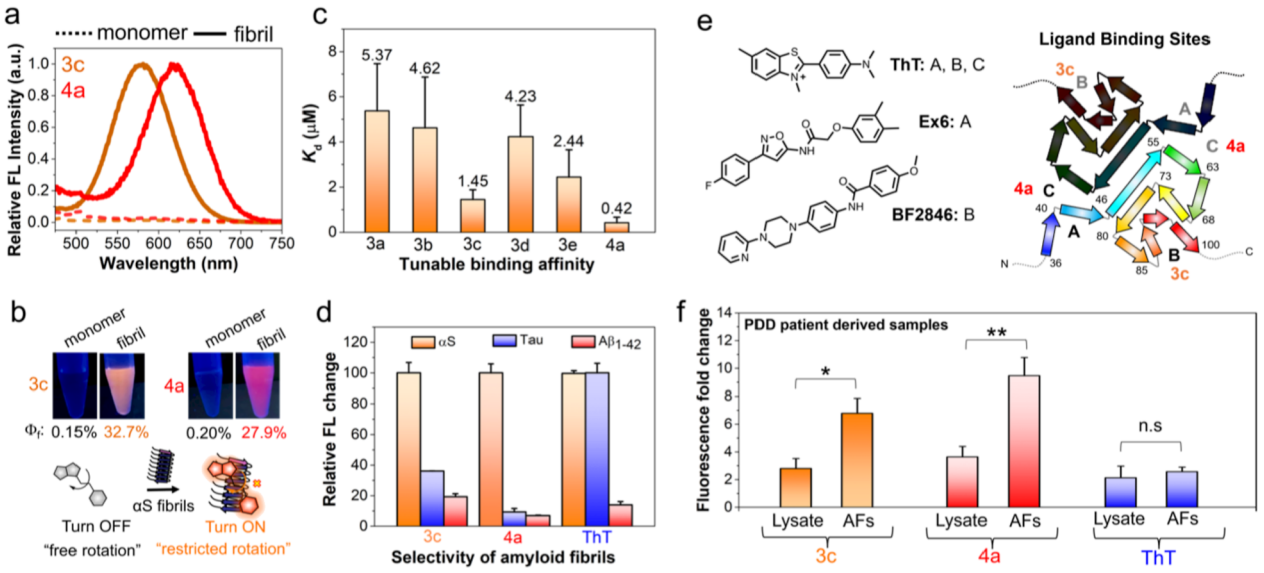

Figure 4. Structural modification affects probe detection of amyloid fibrils. (a) Fluorescence spectral changes of probes **3c** and **4a** (10 μM) in the presence of the αS monomer and fibrils (50 μM). (b) Top: photographs of the **3c** and **4a** (10 μM) in the presence of αS monomer and fibrils (50 μM) under a hand-held UV lamp at 365 nm; bottom: schematic representation of the "turn on" fluorescence of **3c** and **4a** probes upon binding to αS fibrils, resulting from the restricted internal rotation. (c) Tunable dissociation constant (K_d) of **3a**−**e** and **4a** (10 nM−10 μM) with 100 μM αS fibrils. (d) Enhanced amyloid selectivity of the probe **4a** for αS fibrils compared to the **3c** and standard amyloid binding dye ThT (1 μM) among different amyloid fibrils of tau and Aβ_{1-42} that are present in patients with neurodegenerative diseases. (e) Binding sites for known ligands based on cryo-EM (ThT)[30] and photo-cross-linking (Ex6 and BF2846) shown on top-down view of two-stranded fibril with residues numbered.[31,32] (f) Fluorescence fold change of probes **3c**, **4a**, and ThT (1 μM) with brain lysates and amplified fibrils (AFs) (1 μM) derived from PDD patients. The bar graph represents the average data of three different PDD patient-derived AFs and lysates. Fold change was subjected to subtraction of free probe fluorescence in PBS buffer. Ex/Em wavelengths: 463/580 nm for **3c**, 484/620 nm for **4a**, and 450/482 nm for ThT. Error bars represent the SD of 3 measurements. Statistical analysis: *p < 0.01 and **p < 0.005.

relationship between fluorescence intensity and viscosity, for newly synthesized RBFs **3b**, **3d**, **3e**, and **4a**, as well as previously known compounds **3a** and **3c**. Fluorescence intensity was measured in binary mixtures of ethylene glycol and glycerol (EG/G) with known viscosities ranging from 16 to 851 cP (cP). The EG/G mixture was selected because EG and G have closely matched dielectric constants, minimizing polarity effects. An increase in G concentration leads to an increase in fluorescence intensity, and χ_2 values were derived for each RBF using second-order polynomial regression. Higher χ_2 values indicate higher fluorescence intensity changes as a function of the viscosity. RBFs exhibited decreased χ values with increasing electron donation, as observed χ_2 value of 1.0 × 10^{-3} for **3a** (R = NH_2) with 5.4-fold fluorescence intensity change, 0.7 × 10^{-3} for **3b** (R = NHMe, 4.68-fold) and 0.6 × 10^{-3} for **3c** (R = NMe_2, 3.82-fold) (Figures 3e,f, S13−S15, and Table S5). This indicates that the restriction of TICT is the primary cause of its fluorogenic response and sensitivity. It has been previously shown that installing a π-rich alternating bridge in RBFs can produce a high energy barrier.[18] In addition to this, substituent variation from **3a** (R = NH_2) to **3c** (R = NMe_2) enhances ICT, as shown by dipole moment and ESP calculations, which further increases the double bond character across the bridge. Moreover, we observed that **3c** was exclusively fluorescent in crystalline or amorphous solids (**3b**, **3d**, **3e**, and **4a**). This indicates that **3c** (CCDC: 2240198) requires well-ordered π−π stacking (J aggregates, head-to-tail packing) to suppress vibrational or rotational motions and activate fluorescence (Figure S16).[29]

We observed a decreased χ_2 value of 0.5 × 10^{-3} for **3d** (R = Az), yet it exhibited a higher fluorescence turn-on (4.07-fold) compared to **3c** (χ_2 = 0.6 × 10^{-3}, 3.82-fold). The lower χ_2 value of **3d** compared to **3c** is attributed to the increased ICT efficiency of the Az group in the excited state that is evident by its calculated E_{em} and μ_{ES} (2.28 eV and 24.03 D) relative to **3c** (E_{em} = 2.32 eV and μ_{ES} = 23.16 D). The higher fluorescence turn-on of **3d** over **3c** results from reduced nonradiative TICT pathways, whereas the NMe_2 group promotes greater nonradiative decay via TICT. This is reflected in the observed fluorescence QYs, with **3d** at 8.1%, higher than **3c** at 7.3%. Similarly, **3e** (R = Mor) exhibited an increased χ_2 of 0.6 × 10^{-3}, with a fluorescence turn-on of 3.81-fold, comparable to **3d**, due to lower electron donation in the excited state and additional nonradiative decay pathways of the Mor group, as evidenced by its blue-shifted λ_{em} and Φ_f (603 nm, 6.9%) compared to Az (605 nm, 8.1%). Interestingly, **4a** (R = NMe_2) with an extended linker, showed the lowest fluorescence change, around 3-fold, with χ_2 = 0.2 × 10^{-3} (Figure 3e,f), suggesting that not only varying aryl substituents but also incorporating π-rich linkers may significantly affect nonradiative pathways by exhibiting a unique photochemical mechanism.

Our efforts focused on understanding the mechanism regulating the viscosity sensitivity of RBFs. Zhang et al. demonstrated that π-rich linkages alter the internal rotation rate (k_{rot}) between planar and twisted configurations of RBF.[18] Building on this, we hypothesized that substituent variations could further influence k_{rot}. We conceptualized two models: model I with a moderate rotational energy barrier ($E_a > k_BT$) for **3a** (R = NH_2), predicting moderate fluorescence changes when measured in methanol and G mixtures (chosen to enhance viscosity variation) at different temperatures, and model II with high E_a ($\gg k_BT$) for **3c** (R = NMe_2), predicting larger fluorescence changes (Figures 3g and S17). To validate

https://doi.org/10.1021/jacs.4c17933
J. Am. Chem. Soc. 2025, 147, 15115−15125

this hypothesis, we measured the fluorescence intensity of RBFs at varying temperatures and viscosities, selecting compounds **3a** and **3c** to test the effects of their substituents on E_a. As shown in Figures 3h and S17, **3c** exhibited a 2.48-fold fluorescence change between 25 and 42 °C, compared to 2.14-fold for **3a**, aligning with model I for **3a** and model II for **3c**. RBFs with high E_a retain greater fluorescence by inhibiting rotational nonradiative decay, as reflected in QY in CH_3CN: **3a** (1.5%), **3c** (7.3%), and **4a** (13.5%) (Table 1). Consequently, high E_a RBFs exhibit a lower viscosity sensitivity. Our findings also reveal that substituent variations, alongside extended π-conjugation, influence viscosity sensitivity, providing a framework for designing fluorophores with tunable fluorogenicity.

Structure Variation Retains Binding to αS Fibrils with Red Shifted Emission. We previously demonstrated that RBF **3c** (R = NMe_2) selectively binds αS fibrils with a fluorescent turn-on response.[29] Here, we explore how aryl substituents or linker length variations affect polarity, affinity, and selectivity upon binding to αS fibrils. The fluorescence measurements of **3a**, **3b**, **3d**, **3e**, and **4a** with αS fibrils showed turn-on fluorescence with different λ_{max}. Interestingly, RBF **4a** showed red emission at 620 nm with a 383-fold brightness increase and a fluorescence lifetime (τ) of 1.27 ns, while **3c** emitted orange fluorescence at 580 nm with a 476-fold increase and a τ of 2.27 ns upon binding to αS fibrils (Figures 4a,b, S19−S21, and Table S7). The color variation is due to polarity changes resulting from the RBF structural variation, as observed in TD-DFT calculations (Figure 2c). All RBFs showed significant Stokes shifts and enhancements in ε, QY, and τ upon binding (Table S8). We next assessed the binding affinities of **3a**−**e** and **4a**. As shown in Figures 4c and S22, the affinity increased with electron donation from **3a** to **3c**, while **3d** and **3e**, with cyclic amines, showed reduced affinity. Notably, **4a**, with an extended linker (n = 2), displayed a dissociation constant (K_d) of 0.42 ± 0.25 μM—3.5 times higher affinity than **3c** (n = 1), which had a K_d of 1.45 ± 0.43 μM.

Given the higher binding affinities of **3c** and **4a**, we next assessed the probes' selectivity for αS fibrils over tau and amyloid-β ($A\beta_{1-42}$). Distinguishing αS from tau and $A\beta_{1-42}$ is crucial for understanding the overlapping pathologies of AD, PD, and other neurodegenerative disorders. Probe **4a** showed significantly higher selectivity for αS fibrils, with 11 times greater turn-on than for tau fibrils and 15 times more than for $A\beta_{1-42}$ fibrils, while **3c** exhibited 2.8- and 5.2-fold higher turn-on, respectively. Thus, our probes, especially **4a**, demonstrated superior target protein selectivity compared to ThT (Figures 4d and S25).

We sought to elucidate the underlying mechanism for the selectivity of **4a** and **3c** relative to ThT and to each other. Cryo-electron microscopy (cryo-EM) structures and computational modeling have revealed that αS fibrils have multiple β-sheet-rich binding pockets with varying affinities for aromatic ligands resembling **3c** and **4a** (Figure 4e).[33] The highest affinity interaction for ThT, which is modeled into the reported cryo-EM structures, involves binding in a pocket formed around Tyr39.[30] In our efforts to develop positron emission tomography imaging probes for αS fibrils in PD and multiple system atrophy (MSA), we have observed binding of aromatic ligands to this site as well, as determined by photo-cross-linking and mass spectrometry experiments.[31,32,34] We refer to this site here as Site A. For a different set of ligands, we have observed selective binding to a site formed around Phe94, which we refer to here as Site B.[31,35] Site B is identified in initial cryo-EM density as a weaker binding site for ThT as well as B227a and C05-03, aromatic ligands with extended π-linkages similar to our RBF compounds.[30] The cryo-EM maps also show density for binding of ThT, B227a, and C05-03 at the fibril−fibril interface (Site C).

To better understand the binding of **3c** and **4a**, we performed competition binding studies with ThT, Ex6, and BF2847. Ex6 and BF2847 have been identified as high affinity, selective Site A and Site B binders, respectively, based on photo-cross-linking studies and low overlap in competitive binding studies.[31,33,34] We found that both **3c** and **4a** competed with the promiscuous binder ThT, but that some ThT emission remained at saturating concentrations, indicating that there was at least one nonoverlapping binding site for each ligand (Figure S23). RBF **3c** binding was not displaced by Ex6 but was partially displaced by BF2846 (Figure S23). Taken together, these data suggest that the fluorescing **3c** species binds at Site B but not at Site A, allowing ThT to remain bound at Site A. In contrast, RBF **4a** fluorescence was not affected by either Ex6 or BF2846, implying that the fluorescence species binds at neither Site A nor Site B (Figure S23). Note that **4a** must have some binding at these sites in order to displace ThT, but these do not seem to activate **4a** fluorescence turn-on. Finally, to ensure that **3c** and **4a** did not bind to regions unresolved in the cryo-EM structures, we performed fluorescence titrations with truncated αS_{1-100} fibrils, omitting the C-terminal region (residues 101−140). It has been shown by cryo-EM that this region can be removed without affecting fibril morphology or fibril−fibril packing.[36] For both **3c** and **4a**, we found results similar to those from our titrations with full length fibrils (Figure S28). Taken together, these results indicate that **3c** and **4a** have several weak binding sites that overlap with ThT, but they have well-defined, fluorogenic sites that are not displaced by ThT (Figure 4e). For RBF **3c**, this site appears to be Site B. For RBF **4a**, this site appears to be neither Site A nor Site B but may be the interfacial site identified in cryo-EM density maps for ThT, B227a, and C05-03 (Site C).

Additional analysis of concentration-dependent binding shows λ_{em} for **4a** shifting from 617 to 618 nm and a larger 6 nm shift for **3c** (from 575 to 581 nm) as the concentration increased (Figure S27), supporting the idea of multiple weak binding sites for **3c** and one site that is primarily responsible for the fluorescent species for **4a**. By using the fits to the λ_{em} values determined in various solvents (Figure S10), one can calculate the dielectric constant of the local environments for **3c** and **4a** bound to αS fibrils. The values obtained for **3c** (35.9 using 581 nm) and **4a** (27.6 using 617 nm) correspond to **3c** binding in a more polar, dimethylformamide-like environment (36.7),[37] while **4a** binds in an ethanol-like environment (24.6).[37] This further supports the idea that the two compounds bind at distinct sites, with the **4a** binding site being more solvent-exposed.

4a Enhances Selectivity for Diagnostic Detection of AFs Derived from Brains of Patients with PDD. We next aimed to explore the clinical potential of **4a**, which shows the greatest in vitro selectivity for αS fibrils over tau and $A\beta_{1-42}$ fibrils. Recent studies have identified unique αS fibril polymorphs linked to diseases that differ from in vitro forms.[21,38,39] Fibril amplification assays hold promise as PD biomarkers, but ThT cannot detect AFs. AFs can be reliably

https://doi.org/10.1021/jacs.4c17933
J. Am. Chem. Soc. 2025, 147, 15115−15125

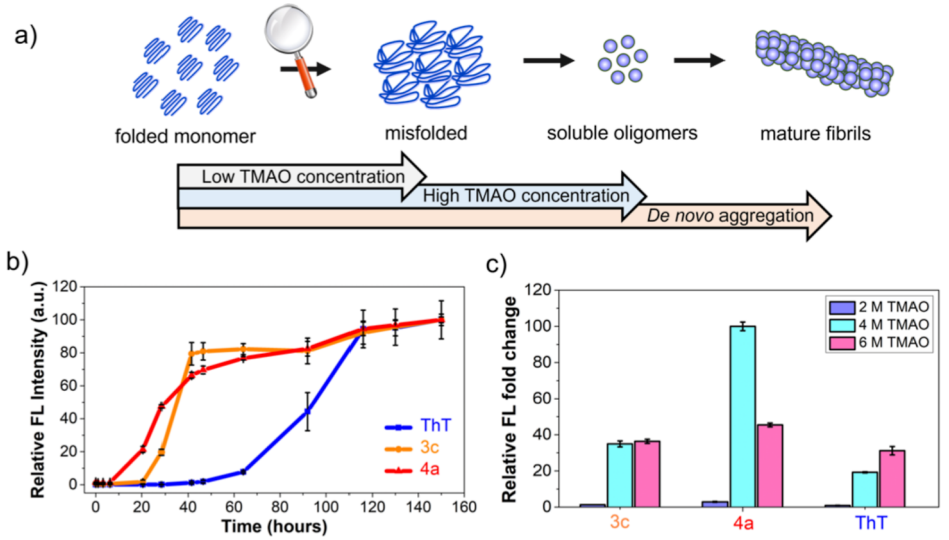

Figure 5. RBFs with extended linkages enable the detection of early misfolding and oligomers formation in vitro. (a) Schematic representation of the stepwise pathway for the formation of αS mature fibrils and αS misfolding or oligomer formation induced by varied TMAO concentration. (b) Monitoring the αS aggregation over prolonged periods using **3c**, **4a**, and ThT in PBS buffer at 37 °C. (c) Fluorescence fold change of RBFs **3c** and **4a** compared to ThT with αS/TMAO solutions (50 μM of αS monomer and 2, 4, and 6 M of TMAO). The fluorescence fold change was determined relative to the fluorescence of the free probe in Tris buffer that contains 2, 4, and 6 M TMAO. Probes were used at a final concentration of 10 μM, mixed with 50 μM αS monomer. Ex/Em wavelengths: 463 nm/580 nm for **3c**, 484 nm/620 nm for **4a**, and 450 nm/482 nm for ThT. Error bars represent the SD of 3 measurements.

amplified in vitro using patient-derived seeds and a recombinant αS monomer. We previously showed **3c** can detect AFs in PD with dementia (PDD).[29] Here, we investigated how structural modification from **3c** to **4a** affects the sensitivity and selectivity of patient-derived αS fibril strains. Notably, **4a** showed 2.6-fold higher fluorescence with PDD-derived AFs ($p < 0.005$) compared to unamplified material (lysate), while **3c** showed 2.4-fold fluorescence increase ($p < 0.01$). ThT failed to distinguish AFs from lysate (Figure 4f). These results suggest that extending the linkages could be a general strategy to improve both sensitivity and selectivity. Specifically, **4a**, with its enhanced selectivity for αS fibrils, shows strong potential for use in a biomarker assay for PD.

RBFs with Extended Linkages Enable the Early Detection of Low-Viscosity αS Misfolding or Oligomer Formation. Current PD treatments focus on alleviating symptoms but do not slow or halt disease progression. A major barrier in PD research is the lack of diagnostic tools for early detection and biochemical monitoring of progression.[40] αS aggregation is a stepwise process, initiated by monomer misfolding, followed by the formation of low-viscosity soluble oligomers, and ultimately leading to high-viscosity insoluble aggregates (Figure 5a).[41,42] While many probes reported thus far have focused on detecting mature fibrils, there are some reports that specifically target oligomers, albeit without specificity for αS.[17] A particular focus on the development of tools to study early aggregation could significantly enhance our understanding of PD progression. Toward addressing this challenge, we monitored αS aggregation using **3c** and **4a** with varying viscosity sensitivity under prolonged agitation. Figure 5b shows that probe **4a** exhibited a 15-fold increase in fluorescence intensity within 20 h, indicating detection of misfolding or oligomers/protofibrils. On the other hand, probe **3c**, although unable to detect changes within 20 h, showed an increase by 40 h, indicating better resolution for later stage oligomers or protofibrils. In contrast, ThT, could not detect either misfolding or oligomers/protofibrils accumulating between 0 and 40 h, only tracking mature fibrils. Moreover, spectra recorded at different time intervals indicate that **4a** exhibits significant fluorescence as early as 8 h of aggregation. At this time point, **3c** shows a minimal signal, and ThT does not show any fluorescence enhancement (Figure S29). These findings suggest that RBFs with higher E_a values (lower χ_2 value, 4a) detect low viscosity early misfolding or oligomers/protofibrils, while those with lower E_a values (higher χ_2 value, 3c) detect later stages and high-viscosity aggregates.

Next, we aimed to study whether these probes with different viscosity sensitivities can differentiate between early misfolding and oligomer formation. To this end, we exposed monomeric αS to varying concentrations of trimethylamine *N*-oxide (TMAO), a natural osmolyte well-known to induce compaction/misfolding at lower [TMAO] and oligomer formation at higher [TMAO] (Figure 5a).[43,44] Interestingly, **4a** exhibits some fluorescence turn-on at 2 M TMAO concentrations, indicating misfolding, with 2.2- and 3.1-fold higher sensitivity than **3c** and ThT, respectively. At 4 M TMAO, **4a** shows the highest turn-on, corresponding to a mixture of misfolding and slight oligomer formation, with 2.9- and 5.2-fold higher sensitivity than **3c** and ThT, respectively. Finally, at 6 M TMAO with significant oligomer formation, **4a** shows similar sensitivity to **3c** and ThT, with just 1.2- and 1.5-fold greater turn-on, respectively (Figure 5c). Together, these results suggest that **4a** exhibits higher selectivity for early misfolding compared with later-stage oligomer formation.

Additionally, we observed distinct λ_{em} values for **4a** with varied TMAO concentrations (Figure S30). The initial red shift in λ_{em} from 604 to 606 nm when TMAO changes from 2 to 4 M suggests an increase in polarity during misfolding, while the blue-shifted λ_{em} of 601 nm at 6 M TMAO indicates a decrease in polarity during oligomer formation. In contrast, **3c** is unable to monitor initial misfolding and only shows sensitivity to oligomer formation, with a decrease in λ_{em} to

https://doi.org/10.1021/jacs.4c17933
J. Am. Chem. Soc. 2025, 147, 15115−15125

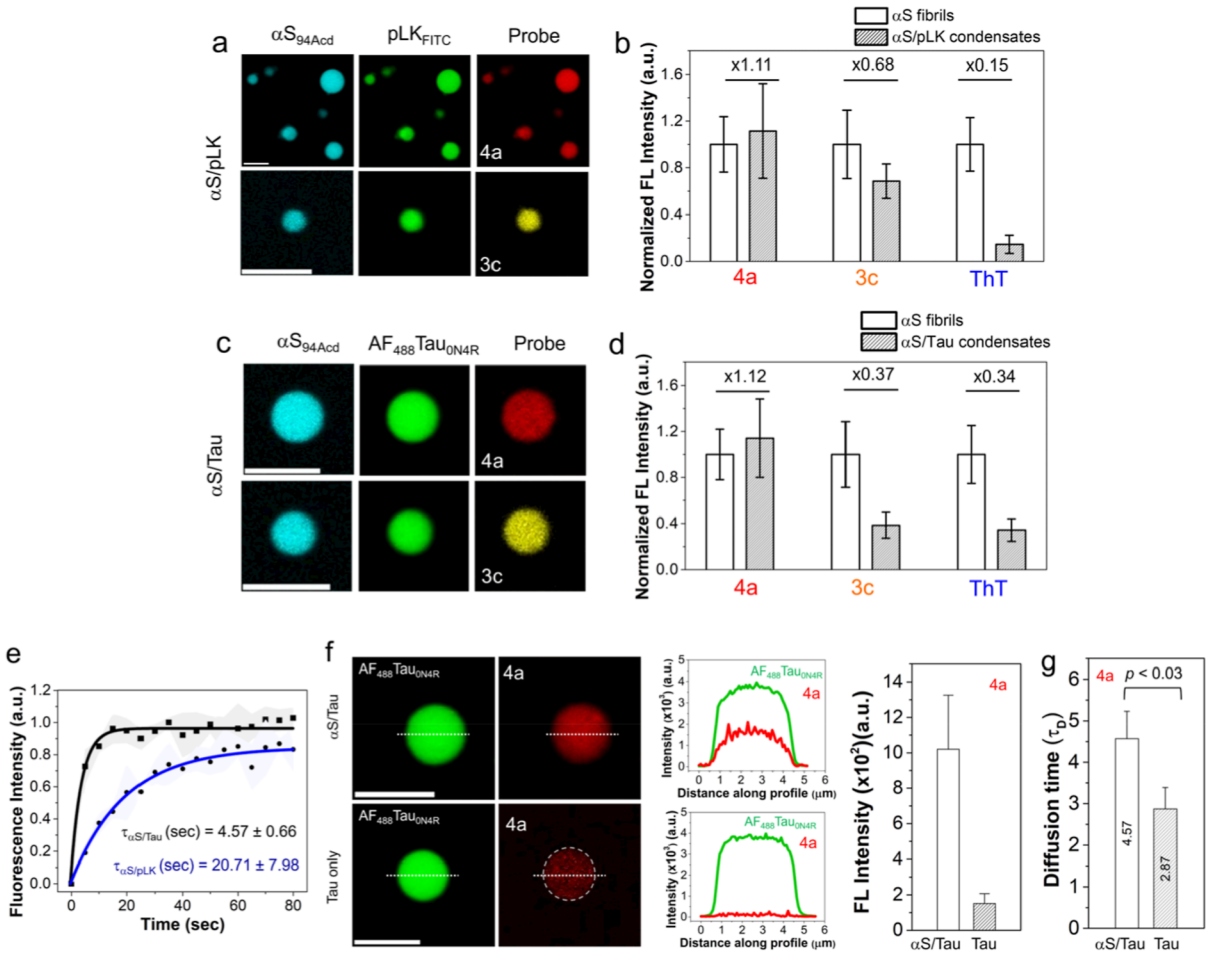

Figure 6. RBFs with extended linkages facilitate fluorescence imaging of αS protein condensates in vitro. (a) Staining of WT αS/pLK (100 μM/0.25 mg/mL) condensates by RBFs **3c** and **4a** in LLPS buffer (doped with 5% FITC-labeled pLK and 5% Acd-labeled αS) using CLSM imaging. (b) Analysis of fluorescence intensity of **3c**, **4a**, and ThT with WT αS/pLK condensates compared with αS fibrils. Ratio of probe intensities (condensates to fibril) shown above the bars. (c) CLSM images of $\alpha S/Tau_{0N4R}$ condensates (80 μM αS and 40 μM tau in LLPS buffer) stained by RBFs **3c**, **4a**, and ThT (doped with 5% AF_{488}-labeled Tau_{0N4R} and 5% Acd-labeled αS). (d) Analysis of staining capacity of **3c**, **4a**, and ThT with $\alpha S/Tau_{0N4R}$ condensates compared to that of αS fibrils. The ratio of intensities, condensate to fibril, shown for each probe. (e) Fluorescence recovery after photobleaching (FRAP) profile showing the translational mobility of αS in αS/pLK and αS/Tau condensates (doped with 5% Acd-labeled αS). (f) Left: CLSM images of condensates of Tau_{0N4R} at a concentration of 40 μM with and without αS (80 μM) in LLPS buffer were stained by **4a** (doped with 5% AF_{488}-labeled Tau_{0N4R}). Middle: fluorescence intensity profile along the dotted white line shows higher fluorescence intensity for Tau_{0N4R} condensates with αS than without αS. Right: analysis of the fluorescence intensity of **4a** with Tau_{0N4R} condensates with and without αS. (g) Comparing the diffusion time (t_D) of $\alpha S/Tau_{0N4R}$ and Tau_{0N4R} only condensates (doped with 5% AF_{488}-labeled Tau_{0N4R}). Error bars represent the standard deviation of >3 measurements. Ex: 488 nm and Em: 500−540 nm for $AF_{488}Tau_{0N4R}$, Ex: 561 nm and Em: 570−620 nm for **3c**, Ex: 561 nm and Em: 630−680 nm for **4a**, and Ex: 405 nm and Em: 430−480 nm for ThT and Acd-labeled αS. All experiments were performed in an LLPS buffer: 20 mM HEPES, 150 mM NaCl, and 1 mM TCEP at pH 7.4, with 15% PEG-8000, at room temperature. Scale bars are 5 μm.

566 to 560 nm at 4 and 6 M TMAO, respectively (Figure S31). These findings indicate that **4a** can be used to study the early stages of PD.

RBFs with Extended Linkages Facilitate Fluorescence Imaging of αS Protein Condensates In Vitro. Studying biomolecular condensates typically requires protein labeling with genetically encoded tags (e.g., green fluorescent protein, HaloTag, and SNAP-Tag) or chemical conjugation of small organic dyes.[45,46] Given the sensitivity of our RBF probes to low viscosity aggregates, we tested their ability to detect unmodified αS in protein condensates.

αS is known to undergo LLPS through electrostatic interaction of its negatively charged C-terminal region with positively charged poly-L-lysine (pLK).[47] We used a three-color imaging strategy to study the staining of αS (100 μM)/pLK (0.25 mg/mL) condensates by RBFs. The condensates contained 5% fluorescently labeled αS at position 94 with acridon-2-yl alanine (Acd, termed αS_{94Acd}) and 5% pLK labeled with fluorescein isothiocyanate (FITC, termed pLK_{FITC}). αS/pLK condensate formation was confirmed by confocal laser scanning microscopy (CLSM) of the Acd signal in the 430−480 nm channel for αS and the 500−540 nm channel for FITC-pLK (Figure 6a). Excitingly, we observed fluorescence signal of our RBFs within the condensates (570−620 nm channel for **3c** and the 630−680 nm channel for **4a**) (Figure 6a).

Next, we analyzed the staining efficiency of **3c**, **4a**, and ThT for αS/pLK LLPS condensates relative to that of αS fibrils (Figures 6b and S33). RBF **4a** exhibited the highest staining efficiency (1.11-fold), followed by **3c** (0.68-fold), while ThT

https://doi.org/10.1021/jacs.4c17933
J. Am. Chem. Soc. 2025, 147, 15115−15125

showed minimal staining (0.15-fold) in the LLPS condensates but excellent staining of fibrils, consistent with our in vitro aggregation kinetics and TMAO experiments. In addition, we observed that **4a**, having low viscosity sensitivity, showed the highest staining of condensates compared to fibrils.

Following these proof-of-concept experiments, we explored αS/tau protein condensates due to recent studies showing that these proteins are known to interact and mutually promote aggregation in vitro and in vivo, indicating potential cross-talk of these two proteins in AD, PD, and related dementias. To test the enrichment of RBFs for αS/tau protein condensates (80 μM/40 μM), we labeled the 0N/4R tau isoform of tau with Alexa Fluor 488 (referred to as $AF_{488}Tau_{0N4R}$) along with labeled αS_{94Acd}. We employed a three-color imaging strategy to confirm the successful incorporation and fluorescence of the RBFs. As shown in Figure 6c, αS/tau condensate formation was confirmed using 5%-labeled αS_{94Acd} and $AF_{488}Tau_{0N4R}$ via CLSM, with the 430−480 nm channel for αS and the 500−540 nm channel for tau (Figure 6c). RBF fluorescence was observed in the 570−620 nm channel for **3c** and the 630−680 nm channel for **4a** (Figure 6c). Moreover, we assessed the fluorescence of **3c**, **4a**, and ThT for αS/tau condensates in comparison to αS fibrils imaged under the same settings. As shown in Figure 6d, RBF **4a** exhibited the highest staining ability, with a 1.12-fold increase for the αS/Tau condensates. In contrast, RBF **3c** demonstrated reduced staining capacity (0.37-fold), similar to that of ThT (0.34-fold) (Figure S34).

The difference in the staining efficacy of **3c** between αS/pLK and αS/Tau condensates was further investigated using FRAP.[48] FRAP revealed that αS/pLK condensates exhibit gel-like properties having diffusion time (τ_D) around 20.71 ± 7.98 s, while αS/tau condensates display liquid-like behavior with τ_D around 4.57 ± 0.66 s (Figures 6e and S35). Nevertheless, **4a** showed more diffuse staining of condensates than **3c**, which showed punctate staining. This difference likely results from the lower viscosity sensitivity of **4a**, allowing it to stain regions of varying viscosity, whereas the higher viscosity sensitivity of **3c** restricts its staining to the more viscous regions of the condensates (Figure S36).[49] Together, these findings suggest that **4a** holds promise for studying liquid-like αS/tau condensates and understanding their molecular interplay and early coaggregation mechanisms, whereas **3c** is more responsive to gel-like or solid-like structures, characteristic of later-stage aggregation species.

RBF **4a** has shown high in vitro selectivity for αS fibrils, so we sought to determine whether probe **4a** also exhibits selectivity for αS condensates over tau condensates. To test this, we prepared Tau_{0N4R} condensates (5% AF_{488}-labeled Tau_{0N4R}) with and without WT αS and assessed the incorporation of **4a** using a two-color imaging strategy via CLSM. Excitingly, **4a** exhibited minimal staining in tau-only condensates but showed strong fluorescence in αS/tau condensates, as observed in the 630−680 nm channel (Figure 6f). Analysis revealed a 3.8-fold higher fluorescence of **4a** into αS-containing tau condensates compared to tau-only condensates (Figure 6f). FRAP experiments further confirmed that tau-only condensates have a lower τ_D (2.87 ± 0.52 s) compared to αS/Tau condensates (4.57 ± 0.66 s), indicating that selectivity of **4a** for αS/Tau was attributed to the high viscosity activated fluorescence compared to that of the tau only condensates (Figures 6g and S35). Collectively, these results demonstrate that probe **4a** can selectively stain αS condensates and holds promise for combined use with labeled tau to advance our understanding of the molecular mechanisms driving complex neurodegenerative diseases.

CONCLUSIONS

In summary, we have shown that incorporating extended π-rich linkages and further changing the electron donation of aryl substituents on bimane chromophores provides a general approach to modulate the photophysical properties, polarity, viscosity sensitivity, and target selectivity of RBFs. These chemical modifications on RBFs result in a D−π−A framework that features (1) red-shifted photophysical properties with large Stokes shifts and (2) high control of the viscosity sensitivity through increased E_a between their planar fluorescent and twisted dark forms, as well as control of the polarity sensitivity through increased ICT.

RBFs with varied aryl substitution or linker lengths exhibit (1) tunable binding affinity and (2) fluorescent turn-on with distinct emission colors due to polarity shifts, supported by TD-DFT-calculated fluorescence energies, ESP maps, and observed dipole moments. Additionally, RBFs with an extended linker length not only showed high selectivity for αS fibrils in vitro over other amyloid fibrils such as tau and $A\beta_{1-42}$ but also patient-derived AFs of PDD. Mechanistic studies further reveal that the high selectivity of RBF **4a** stems from its specific binding to high-affinity sites, while **3c** binds nonspecifically to multiple sites.

RBF **4a**, with lower viscosity sensitivity, detects early misfolding and αS protein oligomers, whereas RBF **3c** is sensitive to later-stage species like oligomers. In contrast, the standard amyloid-binding dye ThT detects only mature fibrils. These findings align with TMAO-based fluorescence measurements, highlighting RBF **4a** as a superior probe for studying early stages of PD. Finally, we showed for the first time the use of small molecule-based fluorescent probes for selective imaging of phase-separated αS. Chemical modifications provide RBFs **3c** and **4a** with tailored viscosity sensitivity, enabling successful staining of αS/pLK and αS/tau condensates. Notably, RBF **4a** showed selective imaging of αS condensates over tau condensates. Thus, **4a** complements other RBFs that are useful for selective imaging of αS fibrils, such as **Tg-52**, which has been shown to have specificity toward αS in PD over MSA.[16]

We anticipate that the environmental sensitivity and tunable properties of RBFs **3c** and **4a** may open avenues for various applications in biology and materials chemistry. As shown in Figure S12, RBF **4a** demonstrated higher sensitivity to low-polarity environments, making it a promising probe for studying the local polarity of cellular components or microenvironments in biological tissues. Additionally, RBFs **3c** and **4a**, with distinct sensitivity to high and low viscosities, respectively, can be combined to investigate the molecular mechanisms of αS aggregation, which progresses through a stepwise process from low-viscosity misfolded oligomers to high-viscosity mature fibrils. As shown in Figure S37, bleed-through experiments with **3c** and **4a** confirmed no emission overlap with the Alexafluor 488 fluorophore channels when they were excited at 488 nm. This suggests that **3c** and **4a** can be effectively combined with the Alexafluor 488 probe to study proteins interacting with αS pathology such as tau. In another example, these probes exhibit high fluorescence in the crystalline state, as shown in Figure S16, indicating their potential for use in organic materials. We will explore all of these applications in future studies.

https://doi.org/10.1021/jacs.4c17933
J. Am. Chem. Soc. 2025, 147, 15115−15125

■ ASSOCIATED CONTENT

Supporting Information

The Supporting Information is available free of charge at https://pubs.acs.org/doi/10.1021/jacs.4c17933.

Detailed procedures for small molecule synthesis, structural, and photophysical characterization; protein expression and fibril formation, computational analysis, and binding assays (PDF)

■ AUTHOR INFORMATION

Corresponding Authors

Yarra Venkatesh − *Department of Chemistry, University of Pennsylvania, Philadelphia, Pennsylvania 19104, United States;* orcid.org/0000-0002-4478-1553; Email: venkyy@sas.upenn.edu

E. James Petersson − *Department of Chemistry, University of Pennsylvania, Philadelphia, Pennsylvania 19104, United States; Department of Biochemistry and Biophysics, Perelman School of Medicine, University of Pennsylvania, Philadelphia, Pennsylvania 19104, United States;* orcid.org/0000-0003-3854-9210; Email: ejpetersson@sas.upenn.edu

Authors

Karthik B. Narayan − *Department of Chemistry, University of Pennsylvania, Philadelphia, Pennsylvania 19104, United States;* orcid.org/0000-0003-1047-0375

Tobias Baumgart − *Department of Chemistry, University of Pennsylvania, Philadelphia, Pennsylvania 19104, United States;* orcid.org/0000-0001-7385-8460

Complete contact information is available at: https://pubs.acs.org/10.1021/jacs.4c17933

Notes

The authors declare no competing financial interest.

■ ACKNOWLEDGMENTS

This research was supported by the National Institutes of Health (NIH U19-NS110456 to E.J.P. and RF1-NS103873 to E.J.P.). Instruments supported by the NIH and NSF include NMR (NSF CHE-1827457), mass spectrometers (NIH RR-023444 and NIH S10-OD030460), and a computing cluster (NIH S10-OD023592). V.Y. and E.J.P. thank Virginia Lee and Nicholas Marotta for amplified fibrils from PDD patient samples, Robert Mach and Ryann Perez, respectively, for contributing BF2846 and Ex6, and Honey Priya James for help with FRAP.

■ REFERENCES

(1) Jun, J. V.; Chenoweth, D. M.; Petersson, E. J. Rational design of small molecule fluorescent probes for biological applications. *Org. Biomol. Chem.* **2020**, *18* (30), 5747−5763.

(2) Lavis, L. D.; Raines, R. T. Bright Ideas for Chemical Biology. *ACS Chem. Biol.* **2008**, *3* (3), 142−155.

(3) Terai, T.; Nagano, T. Fluorescent probes for bioimaging applications. *Curr. Opin. Chem. Biol.* **2008**, *12* (5), 515−521.

(4) Hoelzel, C. A.; Zhang, X. Visualizing and Manipulating Biological Processes by Using HaloTag and SNAP-Tag Technologies. *ChemBioChem* **2020**, *21* (14), 1935−1946.

(5) Le, P.; Ahmed, N.; Yeo, G. W. Illuminating RNA biology through imaging. *Nat. Cell Biol.* **2022**, *24* (6), 815−824.

(6) Wang, M.; Da, Y.; Tian, Y. Fluorescent proteins and genetically encoded biosensors. *Chem. Soc. Rev.* **2023**, *52* (4), 1189−1214.

(7) Speight, L. C.; Samanta, M.; Petersson, E. J. Minimalist Approaches to Protein Labelling: Getting the Most Fluorescent Bang for Your Steric Buck. *Aust. J. Chem.* **2014**, *67* (5), 686−700.

(8) Sasaki, S.; Drummen, G. P. C.; Konishi, G.-i. Recent advances in twisted intramolecular charge transfer (TICT) fluorescence and related phenomena in materials chemistry. *J. Mater. Chem. C* **2016**, *4* (14), 2731−2743.

(9) Haidekker, M. A.; Theodorakis, E. A. Molecular rotors—fluorescent biosensors for viscosity and flow. *Org. Biomol. Chem.* **2007**, *5* (11), 1669−1678.

(10) Paez-Perez, M.; Kuimova, M. K. Molecular Rotors: Fluorescent Sensors for Microviscosity and Conformation of Biomolecules. *Angew. Chem., Int. Ed.* **2024**, *63* (6), No. e202311233.

(11) Louros, N.; Schymkowitz, J.; Rousseau, F. Mechanisms and pathology of protein misfolding and aggregation. *Nat. Rev. Mol. Cell Biol.* **2023**, *24* (12), 912−933.

(12) Giehm, L.; Otzen, D. E. Strategies to increase the reproducibility of protein fibrillization in plate reader assays. *Anal. Biochem.* **2010**, *400* (2), 270−281.

(13) Naiki, H.; Higuchi, K.; Hosokawa, M.; Takeda, T. Fluorometric determination of amyloid fibrils in vitro using the fluorescent dye, thioflavin T1. *Anal. Biochem.* **1989**, *177* (2), 244.

(14) Coelho-Cerqueira, E.; Pinheiro, A. S.; Follmer, C. Pitfalls associated with the use of Thioflavin-T to monitor anti-fibrillogenic activity. *Bioorg. Med. Chem. Lett.* **2014**, *24* (14), 3194−3198.

(15) Stsiapura, V. I.; Maskevich, A. A.; Kuzmitsky, V. A.; Uversky, V. N.; Kuznetsova, I. M.; Turoverov, K. K. Thioflavin T as a Molecular Rotor: Fluorescent Properties of Thioflavin T in Solvents with Different Viscosity. *J. Phys. Chem. B* **2008**, *112* (49), 15893−15902.

(16) Lengyel-Zhand, Z.; Ferrie, J. J.; Janssen, B.; Hsieh, C.-J.; Graham, T.; Xu, K.-y.; Haney, C. M.; Lee, V. M. Y.; Trojanowski, J. Q.; Petersson, E. J.; Mach, R. H. Synthesis and characterization of high affinity fluorogenic α-synuclein probes. *Chem. Commun.* **2020**, *56* (24), 3567−3570.

(17) Aliyan, A.; Cook, N. P.; Martí, A. A. Interrogating Amyloid Aggregates using Fluorescent Probes. *Chem. Rev.* **2019**, *119* (23), 11819−11856.

(18) Ye, S.; Zhang, H.; Fei, J.; Wolstenholme, C. H.; Zhang, X. A General Strategy to Control Viscosity Sensitivity of Molecular Rotor-Based Fluorophores. *Angew. Chem., Int. Ed.* **2021**, *60* (3), 1339−1346.

(19) Jung, K. H.; Kim, S. F.; Liu, Y.; Zhang, X. A Fluorogenic AggTag Method Based on Halo- and SNAP-Tags to Simultaneously Detect Aggregation of Two Proteins in Live Cells. *ChemBioChem* **2019**, *20* (8), 1078−1087.

(20) Wan, W.; Zeng, L.; Jin, W.; Chen, X.; Shen, D.; Huang, Y.; Wang, M.; Bai, Y.; Lyu, H.; Dong, X.; Gao, Z.; Wang, L.; Liu, X.; Liu, Y. A Solvatochromic Fluorescent Probe Reveals Polarity Heterogeneity upon Protein Aggregation in Cells. *Angew. Chem., Int. Ed.* **2021**, *60* (49), 25865−25871.

(21) Pancoe, S. X.; Wang, Y. J.; Shimogawa, M.; Perez, R. M.; Giannakoulias, S.; Petersson, E. J. Effects of Mutations and Post-Translational Modifications on α-Synuclein In Vitro Aggregation. *J. Mol. Biol.* **2022**, *434* (23), 167859.

(22) Shimogawa, M.; Petersson, E. J. New strategies for fluorescently labeling proteins in the study of amyloids. *Curr. Opin. Chem. Biol.* **2021**, *64*, 57−66.

(23) Mukherjee, S.; Sakunthala, A.; Gadhe, L.; Poudyal, M.; Sawner, A. S.; Kadu, P.; Maji, S. K. Liquid-liquid Phase Separation of α-Synuclein: A New Mechanistic Insight for α-Synuclein Aggregation Associated with Parkinson's Disease Pathogenesis. *J. Mol. Biol.* **2023**, *435* (1), 167713.

(24) Ray, S.; Singh, N.; Kumar, R.; Patel, K.; Pandey, S.; Datta, D.; Mahato, J.; Panigrahi, R.; Navalkar, A.; Mehra, S.; Gadhe, L.; Chatterjee, D.; Sawner, A. S.; Maiti, S.; Bhatia, S.; Gerez, J. A.; Chowdhury, A.; Kumar, A.; Padinhateeri, R.; Riek, R.; Krishnamoorthy, G.; Maji, S. K. α-Synuclein aggregation nucleates through liquid-liquid phase separation. *Nat. Chem.* **2020**, *12* (8), 705−716.

(25) Sawner, A. S.; Ray, S.; Yadav, P.; Mukherjee, S.; Panigrahi, R.; Poudyal, M.; Patel, K.; Ghosh, D.; Kummerant, E.; Kumar, A.; Riek, R.; Maji, S. K. Modulating α-Synuclein Liquid-Liquid Phase Separation. *Biochemistry* **2021**, *60* (48), 3676−3696.
(26) Roy, A.; Oded, B.-E.; Roy, N. C.; Grynszpan, F. Bimanes in retrospect: An in-depth analysis of their chemical evolution and applications of derivatives over the last half century. In *Advances in Heterocyclic Chemistry*; Academic Press, 2025.
(27) Kosower, E. M.; Pazhenchevsky, B.; Hershkowitz, E. 1,5-Diazabicyclo[3.3.0]octadienediones (9,10-dioxabimanes). Strongly fluorescent syn isomers. *J. Am. Chem. Soc.* **1978**, *100* (20), 6516−6518.
(28) Baba, M.; Nakajo, S.; Tu, P. H.; Tomita, T.; Nakaya, K.; Lee, V. M. Y.; Trojanowski, J. Q.; Iwatsubo, T. Aggregation of α-synuclein in Lewy bodies of sporadic Parkinson's disease and dementia with Lewy bodies. *Am. J. Pathol.* **1998**, *152* (4), 879−884.
(29) Venkatesh, Y.; Marotta, N. P.; Lee, V. M. Y.; Petersson, E. J. Highly tunable bimane-based fluorescent probes: design, synthesis, and application as a selective amyloid binding dye. *Chem. Sci.* **2024**, *15* (16), 6053−6063.
(30) Tao, Y.; Xia, W.; Zhao, Q.; Xiang, H.; Han, C.; Zhang, S.; Gu, W.; Tang, W.; Li, Y.; Tan, L.; Li, D.; Liu, C. Structural mechanism for specific binding of chemical compounds to amyloid fibrils. *Nat. Chem. Biol.* **2023**, *19* (10), 1235−1245.
(31) Ferrie, J. J.; Lengyel-Zhand, Z.; Janssen, B.; Lougee, M. G.; Giannakoulias, S.; Hsieh, C.-J.; Pagar, V. V.; Weng, C.-C.; Xu, H.; Graham, T. J. A.; Lee, V. M. Y.; Mach, R. H.; Petersson, E. J. Identification of a nanomolar affinity α-synuclein fibril imaging probe by ultra-high throughput in silico screening. *Chem. Sci.* **2020**, *11* (47), 12746−12754.
(32) Janssen, B.; Tian, G.; Lengyel-Zhand, Z.; Hsieh, C.-J.; Lougee, M. G.; Riad, A.; Xu, K.; Hou, C.; Weng, C.-C.; Lopresti, B. J.; Kim, H. J.; Pagar, V. V.; Ferrie, J. J.; Garcia, B. A.; Mathis, C. A.; Luk, K.; Petersson, E. J.; Mach, R. H. Identification of a Putative α-synuclein Radioligand Using an in silico Similarity Search. *Mol. Imaging Biol.* **2023**, *25* (4), 704−719.
(33) Hsieh, C.-J.; Ferrie, J. J.; Xu, K.; Lee, I.; Graham, T. J. A.; Tu, Z.; Yu, J.; Dhavale, D.; Kotzbauer, P.; Petersson, E. J.; Mach, R. H. Alpha Synuclein Fibrils Contain Multiple Binding Sites for Small Molecules. *ACS Chem. Neurosci.* **2018**, *9* (11), 2521−2527.
(34) Lougee, M. G.; Pagar, V. V.; Kim, H. J.; Pancoe, S. X.; Chia, W. K.; Mach, R. H.; Garcia, B. A.; Petersson, E. J. Harnessing the intrinsic photochemistry of isoxazoles for the development of chemoproteomic crosslinking methods. *Chem. Commun.* **2022**, *58* (65), 9116−9119.
(35) Kim, H. Y.; Chia, W. K.; Hsieh, C.-J.; Saturnino Guarino, D.; Graham, T. J. A.; Lengyel-Zhand, Z.; Schneider, M.; Tomita, C.; Lougee, M. G.; Kim, H. J.; Pagar, V. V.; Lee, H.; Hou, C.; Garcia, B. A.; Petersson, E. J.; O'Shea, J.; Kotzbauer, P. T.; Mathis, C. A.; Lee, V. M. Y.; Luk, K. C.; Mach, R. H. A Novel Brain PET Radiotracer for Imaging Alpha Synuclein Fibrils in Multiple System Atrophy. *J. Med. Chem.* **2023**, *66* (17), 12185−12202.
(36) Ni, X.; McGlinchey, R. P.; Jiang, J.; Lee, J. C. Structural Insights into α-Synuclein Fibril Polymorphism: Effects of Parkinson's Disease-Related C-Terminal Truncations. *J. Mol. Biol.* **2019**, *431* (19), 3913−3919.
(37) Dielectric Constant, https://macro.lsu.edu/howto/solvents/Dielectric%20Constant%20.htm (accessed April 9, 2025).
(38) Fernandes Gomes, B.; Farris, C. M.; Ma, Y.; Concha-Marambio, L.; Lebovitz, R.; Nellgård, B.; Dalla, K.; Constantinescu, J.; Constantinescu, R.; Gobom, J.; Andreasson, U.; Zetterberg, H.; Blennow, K. α-Synuclein seed amplification assay as a diagnostic tool for parkinsonian disorders. *Parkinsonism Relat. Disord.* **2023**, *117*, 105807.
(39) Marotta, N. P.; Ara, J.; Uemura, N.; Lougee, M. G.; Meymand, E. S.; Zhang, B.; Petersson, E. J.; Trojanowski, J. Q.; Lee, V. M. Y. Alpha-synuclein from patient Lewy bodies exhibits distinct pathological activity that can be propagated in vitro. *Acta Neuropathol. Commun.* **2021**, *9* (1), 188.
(40) Watt, K. J. C.; Meade, R. M.; James, T. D.; Mason, J. M. Development of a hydroxyflavone-labelled 4554W peptide probe for monitoring αS aggregation. *Sci. Rep.* **2023**, *13* (1), 10968.
(41) Liu, Y.; Wolstenholme, C. H.; Carter, G. C.; Liu, H.; Hu, H.; Grainger, L. S.; Miao, K.; Fares, M.; Hoelzel, C. A.; Yennawar, H. P.; Ning, G.; Du, M.; Bai, L.; Li, X.; Zhang, X. Modulation of Fluorescent Protein Chromophores To Detect Protein Aggregation with Turn-On Fluorescence. *J. Am. Chem. Soc.* **2018**, *140* (24), 7381−7384.
(42) Wolstenholme, C. H.; Hu, H.; Ye, S.; Funk, B. E.; Jain, D.; Hsiung, C.-H.; Ning, G.; Liu, Y.; Li, X.; Zhang, X. AggFluor: Fluorogenic Toolbox Enables Direct Visualization of the Multi-Step Protein Aggregation Process in Live Cells. *J. Am. Chem. Soc.* **2020**, *142* (41), 17515−17523.
(43) Ferrie, J. J.; Haney, C. M.; Yoon, J.; Pan, B.; Lin, Y.-C.; Fakhraai, Z.; Rhoades, E.; Nath, A.; Petersson, E. J. Using a FRET Library with Multiple Probe Pairs To Drive Monte Carlo Simulations of α-Synuclein. *Biophys. J.* **2018**, *114* (1), 53−64.
(44) Uversky, V. N.; Li, J.; Fink, A. L. Trimethylamine-N-oxide-induced folding of alpha-synuclein. *FEBS Lett.* **2001**, *509* (1), 31.
(45) Pandey, N. K.; Varkey, J.; Ajayan, A.; George, G.; Chen, J.; Langen, R. Fluorescent protein tagging promotes phase separation and alters the aggregation pathway of huntingtin exon-1. *J. Biol. Chem.* **2024**, *300* (1), 105585.
(46) Huang, Y.; Chen, J.; Hsiung, C.-H.; Bai, Y.; Tan, Z.; Ye, S.; Zhang, X. Detecting protein-protein interaction during liquid-liquid phase separation using fluorogenic protein sensors. *Mol. Biol. Cell* **2024**, *35* (3), ar41.
(47) Gracia, P.; Polanco, D.; Tarancón-Díez, J.; Serra, I.; Bracci, M.; Oroz, J.; Laurents, D. V.; García, I.; Cremades, N. Molecular mechanism for the synchronized electrostatic coacervation and co-aggregation of alpha-synuclein and tau. *Nat. Commun.* **2022**, *13* (1), 4586.
(48) Mondal, S.; Narayan, K.; Botterbusch, S.; Powers, I.; Zheng, J.; James, H. P.; Jin, R.; Baumgart, T. Multivalent interactions between molecular components involved in fast endophilin mediated endocytosis drive protein phase separation. *Nat. Commun.* **2022**, *13* (1), 5017.
(49) Kilgore, H. R.; Mikhael, P. G.; Overholt, K. J.; Boija, A.; Hannett, N. M.; Van Dongen, C.; Lee, T. I.; Chang, Y.-T.; Barzilay, R.; Young, R. A. Distinct chemical environments in biomolecular condensates. *Nat. Chem. Biol.* **2024**, *20* (3), 291−301.

https://doi.org/10.1021/jacs.4c17933
J. Am. Chem. Soc. 2025, 147, 15115−15125